Journal of Magnetic Resonance **156,** 41–51 (2002)
doi:10.1006/jmre.2002.2526

# Enhanced Signal Intensities Obtained by Out-of-Phase Rapid-Passage EPR for Samples with Long Electron Spin Relaxation Times

James R. Harbridge, George A. Rinard, Richard W. Quine, Sandra S. Eaton, and Gareth R. Eaton[1]

*Department of Engineering and Department of Chemistry and Biochemistry, University of Denver, Denver, Colorado 80208*

Received August 30, 2001; revised March 8, 2002; published online May 31, 2002

**To understand the signals that are observed under rapid-passage conditions for samples with long electron spin relaxation times, the E′ defect in irradiated vitreous $SiO_2$ was studied. For these samples at room temperature, $T_1$ is 200 $\mu$s and $T_2$ ranged from 35 to 200 $\mu$s, depending on spin concentration. At X band with 100-kHz modulation frequency and 1-G modulation amplitude there was minimal lineshape difference between the low-power, in-phase spectra and high-power spectra detected 90° out-of-phase with respect to the magnetic field modulation. Signal enhancement, defined as the ratio of the intensities of the out-of-phase to the in-phase signals when $B_1$ for both observation modes is adjusted to give maximum signal, was 3.4 to 9.5 at room temperature. The origin of the out-of-phase signal was modeled by numerical integration of the Bloch equations including magnetic field modulation. The waveforms for the E′ signal, prior to phase sensitive detection, were simulated by summing the contributions of many individual spin packets. Good agreement was obtained between experimental and calculated waveforms. At low $B_1$ the experimental values of $T_1$ and $T_2$ were used in the simulations. However, at higher $B_1$, $T_2$ was adjusted to match the experimental signal intensity and increased with increasing $B_1$. At high $B_1$, $T_2 = T_1$, consistent with Redfield's and Hyde's models. For the spin concentrations examined, the out-of-phase signals at very high power ($B_1 \sim 0.33$ G) displayed a linear relationship between peak-to-peak signal amplitude and spin concentration. Under the conditions used for spin quantitation the signal-to-noise for these spectra was up to 5 times higher than for the in-phase signal, which greatly facilitates quantitation for these types of samples. For samples in which $T_2$ is dominated by electron spin–spin interaction, lower spin concentration results in longer $T_2$ and the enhancement is increased.** 

## INTRODUCTION

Typically, continuous wave (CW) EPR spectra are obtained under nonsaturating slow-passage conditions where (a) the saturation factor, $s$, defined by Eq. [1] is close to 1 and (b) the rate of change of the magnetic field due to sweep of the external magnetic field, $B_0$, and to magnetic field modulation, $B_m$, is slow relative to the relaxation rates of the spins studied:

$$s = \frac{1}{1 + \gamma^2 B_1^2 T_1 T_2}. \qquad [1]$$

$B_1$ is the microwave magnetic field and $\gamma$ is the gyromagnetic ratio.

"Rapid passage" occurs when the rate of change of $B_0$ or $B_m$ is greater than the electron spin relaxation rate. Portis was the first to interpret EPR spectra in terms of the Bloch rapid-passage model (*1*). Hyde (*2*) confirmed many of the predictions made by Portis (*1*) for rapid-passage dispersion signals and their dependence on modulation amplitude and microwave $B_1$. Rapid-passage effects underlie the saturation-transfer method of measuring molecular motion that was developed by Hyde and Dalton (*3*). Early discussions and background information on these effects are in Refs. (*2, 4–6*).

For many samples of interest relaxation rates are so long that it is difficult to obtain unsaturated slow-passage spectra with adequate signal-to-noise. At room temperature such cases include defect centers in solids, and especially those in solids with few nuclear spins, such as Si (*7*) and $SiO_2$. Some of these samples have important applications in radiation dosimetry, archeological dating, and device technology that make quantitation of the spins important. For most organic radicals, including nitroxyl radicals, relaxation times at 77 K and below are so long that extremely low microwave powers, modulation amplitudes, and modulation frequencies must be used to record spectra that are free of passage effects. Recent examples of the impact of passage effects are spectra of the tyrosyl radical in Photosystem II at 135 and 245 GHz (*8, 9*). At very low temperatures, $T_1$ becomes long enough that even for transition metal complexes it is not possible to obtain unsaturated slow-passage CW EPR spectra (*10*).

Several rapid-passage detection methods have been used to improve signal-to-noise for samples with long relaxation times. The following notation is used in describing these experiments. Detection of the absorption or dispersion signal is selected by setting the phase of the detected signal relative to the phase of the source microwaves. "In-phase" vs "90°-out-of-phase" (or simply "out-of-phase") refers to the phase of the signal relative

[1] To whom correspondence should be addressed at Department of Chemistry and Biochemistry, University of Denver, Denver, CO 80208-2436. E-mail: geaton@du.edu.



1090-7807/02 $35.00

to that of the magnetic field modulation. The component of the signal that varies at the same frequency as the modulation is termed the fundamental and the component that varies at twice the modulation frequency is the 2nd harmonic. Under rapid passage conditions 2nd harmonic signals resemble absorption spectra rather than the 2nd derivative of the absorption signal.

Out-of-phase detection of the fundamental has been used in quartz dating to resolve an E′ signal from an overlapping signal of a peroxy radical center that had different relaxation times (*11*). Griscom and Cook used 2nd harmonic out-of-phase detection at high microwave power to study the $^{29}$Si hyperfine lines for the E′ signal in natural-abundance and $^{29}$Si-enriched $SiO_2$ (*12, 13*). The 2nd harmonic detection 90° out-of-phase also has been used to improve signal-to-noise in tooth dosimetry (*14–16*) at low accumulated dose, and in one case, a fourfold improvement in signal-to-noise was found at 77 K (*14, 16*). The 2nd harmonic detection 90° out-of-phase was used by Clarkson and Leniart to resolve proton hyperfine in the spectra of di-tert butyl nitroxide (*17*). The proton hyperfine was observable because out-of-phase detection is more sensitive than in-phase detection to the different relaxation times of the nuclear spins in the sample. When EPR lines with different relaxation times overlap, the lines are brought into rapid-passage conditions at different microwave powers, so this method provides a means of selectively observing different transitions (*10*). The 2nd harmonic in-phase spectra have been used to study Fe(III) signals at low temperature (*18, 19*). These papers did not address the nature of the out-of-phase signal. The possibility of spin quantitation under rapid passage conditions also has not been addressed.

To better understand the out-of-phase rapid-passage signals we have performed a series of experimental and computational studies of the EPR spectra of the E′ defect signal in irradiated $SiO_2$. Amorphous silicon dioxide ($SiO_2$) is of substantial interest because of its fiber-optic and metal-oxide-semiconductor applications. These devices can be damaged by high-energy radiation that causes defect formation in the $SiO_2$. The dominant defect that persists at room temperature is called the E′ center (*20*). It is assigned as an oxygen vacancy site at which the unpaired electron occupies a dangling $sp^3$ hybrid orbital of a silicon that is bonded to three oxygens. Several groups have characterized E′ centers in amorphous and crystalline $SiO_2$ (*12, 13, 21–28*).

For the E′ signal in irradiated amorphous $SiO_2$ the longitudinal relaxation time, $T_1$, measured by various techniques, varies with position in the spectrum and is approximately 200 $\mu$s at room temperature (*24, 26, 29*). The transverse relaxation times, $T_2$, for the samples examined in the present study are between 35 and 200 $\mu$s. Even at the lowest power available on most commercial EPR spectrometers (20 nW) an E′ signal with $T_1 = 200$ $\mu$s and $T_2 = 30$ $\mu$s has a saturation factor, $s = 0.73$ (Eq. [1]), assuming the resonator produces approximately 1 $G/\sqrt{W}$ of incident microwave power (*30–32*). Because of these long relaxation times the E′ center was selected for this study. The methods presented in this paper are applicable to a wide range of spin systems with long $T_1$ and $T_2$.

Normally CW EPR spectra are obtained by phase-sensitive detection at the frequency of the magnetic field modulation, which selects the fundamental in-phase component of the spin response. In this paper, the signal prior to phase-sensitive detection was recorded and analyzed, which permits analysis of all components whether in-phase or out-of-phase, at the fundamental and all harmonics. To understand the origin of the out-of-phase signals, the time dependence of the responses from individual spin packets with relaxation-determined widths was calculated by numerical solution of the Bloch equations (*4*), incorporating magnetic field modulation. The contributions from many spin packets were then summed to model experimental waveforms prior to phase sensitive detection. The amplitude of a component at a particular frequency in a magnitude Fourier transform of a waveform corresponds to the signal that would be observed by phase-sensitive detection at that frequency, when the phase of the detector is set to match that of the signal. Redfield (*33*), Hyde (*34*), and Feher (*35*) have pointed out that when $B_1$ is large, $T_2$ approaches $T_1$. Redfield therefore proposed that when the Bloch equations are applied to cases with high $B_1$, $T_2$ should be replaced by $T_1$. The appropriate form of the Bloch equations for intermediate values of $B_1$ was not discussed. To achieve a smooth variation of the solutions of the Bloch equations between the low- and high-$B_1$ regimes, we treated $T_2$ as an adjustable parameter that varied from the experimental value at low $B_1$ up to $T_1$ at high $B_1$. The value of $T_2$ was adjusted to match the dependence of EPR signal intensity on $B_1$.

## EXPERIMENTAL

Samples of vitreous $SiO_2$ samples (approximately 2-mm o.d. by 10-mm-long cylinders) were irradiated at 24.4, 5.8, and 0.870 Mrad. The 24.4- and 5.8-Mrad samples were irradiated with $^{60}$Co $\gamma$-rays. The low-dose sample was irradiated with residual radiation from a nuclear reactor, with a dose that was calibrated to be equivalent to a $^{60}$Co dose of 0.870 Mrad. Samples were studied at X band on a Varian E-9 spectrometer equipped with a $TE_{102}$ resonator and a Wilmad quartz Dewar insert. For this resonator the $B_1$ at the sample, determined by measuring the length of a 90° pulse at known incident power on a Bruker E580 spectrometer, was 1.7 $G/\sqrt{W}$. This value compares well with the literature (*30–32*) after accounting for the concentration of the microwaves by the quartz Dewar insert, which increases $B_1/\sqrt{W}$. The samples were centered in the resonator, where the magnitude of $B_1$ varies by only a small amount over the dimensions of the samples. For the three samples, the waveforms prior to phase-sensitive detection were measured at the three magnetic field positions marked in Fig. 1. The EPR signal from the bridge to the console was digitized. Normally, this signal goes to the phase-sensitive detector in the console where the 100-kHz component provides the EPR spectrum. The waveforms were signal-averaged in a Lecroy 9410 digital oscilloscope. A reference signal proportional to the magnetic field modulation was

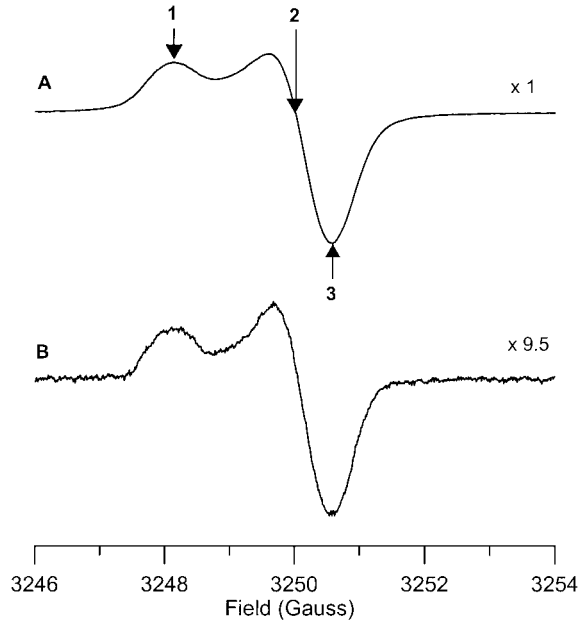


**FIG. 1.** The X band CW spectra of the E′ signal in a $SiO_2$ sample irradiated at 0.87 Mrad. Spectra were obtained at room temperature with 1-G modulation amplitude. Both modulation and phase-sensitive detection were at 100 kHz. (A) Spectrum obtained with $B_1 = 0.14$ G and detected 90° out-of-phase with respect to the modulation. (B) Spectrum obtained at $B_1 = 0.0085$ G and detected in-phase with the modulation. The spectrometer gain setting for spectrum (B) was 9.5 times that for spectrum (A). Waveforms prior to phase-sensitive detection were measured at positions 1, 2, and 3 that are marked on spectrum (A).

obtained with a current sensor attached to the cable that carries the modulation to the resonator.

Relaxation times were measured on a homebuilt spectrometer that was described previously (*36, 37*). Data fitted well to a single exponential. $T_1$ was measured by inversion recovery (180–$T$–90–$\tau$–180–$\tau$–echo pulse sequence) using a $B_1$ that was sufficiently large to ensure that the entire E′ spectrum was excited, in order to eliminate spectral diffusion. $T_2$ relaxation times were measured by the Carr–Purcell–Meiboom–Gill (CPMG) pulse sequence (*38*) and by electron spin-echo dephasing (*29*). In the spin-echo measurements, the echo decay rate constant ($1/T_m$) was measured as a function of pulse turning angle and extrapolated to an infinitely small turning angle. The limiting value of $1/T_m$ was equated to $1/T_2$. For the 24.4- and 5.8-Mrad samples, the two techniques gave $T_2$ values that agreed within 5%. For the 0.87-Mrad sample, the signal-to-noise for the small turning-angle spin-echo experiments was poor and the resulting estimates of $T_2$ were deemed to not be as reliable as the CPMG values.

**TABLE 1**
**Spin Concentrations and Room Temperature Relaxation Times for E′ Signals**

| Radiation dose (Mrad) | Local spin concentration (spins/cm$^3$)[a] | Bulk spin concentration (spins/cm$^3$)[b] | $T_1$[c] ($\mu$s) | $T_2$[d] ($\mu$s) | $B_1$ (G) for maximum out-of-phase signal | Signal enhancement[e] |
|---|---|---|---|---|---|---|
| 0.870 | $1.2 \times 10^{16}$ | $1.6 \times 10^{16}$ | 200 | 200 | 0.14 | 9.5 |
| 5.7 | $1.3 \times 10^{17}$ | $1.4 \times 10^{17}$ | 200 | 63 | 0.19 | 5.0 |
| 24.4 | $3.6 \times 10^{17}$ | $2.8 \times 10^{17}$ | 200 | 35 | 0.23 | 3.4 |

[a] Determined by instantaneous diffusion measurements.
[b] Determined by comparison of double integrals, after correction for saturation, with integrals for a sample of TEMPONE.
[c] Determined by inversion recovery.
[d] Determined by CPMG.
[e] Ratio of the 90° out-of-phase and in-phase signals. For each measurement mode, $B_1$ was adjusted to give maximum signal amplitude.

Local spin concentrations were estimated from the slope of the plot of $1/T_m$ versus turning angle (*29*). Bulk spin concentrations were determined by comparison of double integrals of E′ spectra obtained at the lowest power available on the E-9 (20 nW) with double integrals of spectra for a known-concentration solution of TEMPONE (4-oxo-2,2,6,6-tetramethyl-1-piperidinyloxy). Since the relaxation times for the E′ centers in each of the $SiO_2$ sample were measured, the degree of saturation of the signal could be calculated (Eq. [1]) and the integrals corrected for saturation. The measurements indicated that the local spin concentrations were approximately equal to the bulk spin concentrations (Table 1).

## CALCULATIONS

The Bloch equations, including magnetic field modulation, are

$$\begin{aligned}\frac{dM_u}{dt} &= \frac{-M_u}{T_2} - (\Delta\omega + \Omega_m \cos(\omega_m t))M_v \\ \frac{dM_v}{dt} &= (\Delta\omega + \Omega_m \cos(\omega_m t))M_u - \frac{M_v}{T_2} - \gamma B_1 M_z \\ \frac{dM_z}{dt} &= \frac{M_0}{T_1} + \gamma B_1 M_v - \frac{M_z}{T_1},\end{aligned} \quad [2]$$

where $\gamma$, the electron magnetogyric ratio, $=1.7608 \times 10^7$ rad s$^{-1}$ G$^{-1}$, $\Delta\omega$ is the offset of a spin packet from the center of the modulation, in angular frequency; $\Omega_m$ is the amplitude of the modulation field in angular units, $=0.5\gamma\ B_m$ where $B_m$ is the peak-to-peak modulation amplitude in gauss; $\nu_m$ is the modulation frequency in Hz; $\omega_m$ is the angular modulation frequency $= 2\pi\nu_m$; $M_0$ is the spin magnetization at the position in the spectrum for a particular spin packet; and $B_1$ is the microwave magnetic field in gauss.

The time evolution of the magnetization for a spin packet was evaluated using fourth-order Runge–Kutta numerical integration (*39*). Typically, the numerical integration was performed at 1000 to 3000 points per modulation cycle. Calculations for a single spin packet were performed in Mathcad (MathSoft, Cambridge, MA). Simulations of experimental waveforms

based on the contributions from multiple spin packets were performed in Compaq Visual Fortran. For each spin packet, the relative magnetization, $M_0$, at that position in the spectrum was read from the first integral of an experimental lineshape obtained at low microwave power. Equivalent results were obtained with spin packets spaced equally along the time axis or spaced equally in magnetic field. For spin packets spaced equally along the time axis, their contributions were weighted by $M_0 * \sin(\omega_m t)$ to account for the number of spin packets that would be sampled during the time interval $t + \Delta t$. The time dependence of $M_v$ (the absorption signal) was compared with the experimental waveforms prior to phase-sensitive detection. The calculated and experimental waveforms were Fourier transformed using Mathcad and the magnitude spectra were compared. The phase angle for the fundamental was calculated from the ratio of the imaginary and real components at 100 kHz.

## RESULTS

Table 1 summarizes spin concentrations and electron spin relaxation times for the E′ signal at room temperature. The highest and lowest spin concentrations differ by more than an order of magnitude. Relaxation times were measured at the point in the spectrum where the absorption signal is a maximum (position 2, Fig. 1). $T_1$ values for the three samples were the same, within experimental error. Values of $T_2$ increased with decreasing spin concentration, varying from 35 to 200 $\mu$s. $T_2$ is long compared to values for many proton-containing samples because there are few nuclear spins ($^{29}$Si is 4.7% abundant) in $SiO_2$ to affect the electron spin dephasing time, so the dephasing is dominated by electron–electron interaction (*29, 40*).

Figure 1 displays room temperature CW spectra of the E′ signal from the 0.87-Mrad sample, obtained 90° out-of-phase and in-phase with respect to the magnetic field modulation. Each spectrum was obtained with the $B_1$ that gave the maximum signal for that observation mode (i.e., saturation factor, $s$ (Eq. [1]), <1). After correcting for differences in the gain at which spectra were recorded, the peak-to-peak amplitude of the maximum out-of-phase signal (Fig. 1A) is 9.5 times larger than that for the in-phase signal (Fig. 1B). This ratio of signal amplitudes for the maximum out-of-phase and in-phase signals is defined as the signal enhancement. The noise, after correcting for gain, was the same for the two scans, so this ratio is also the improvement in signal-to-noise that was obtained by recording the spectrum 90° out-of-phase. The $T_2$ relaxation time for this sample at room temperature was 200 $\mu$s (Table 1). The corresponding enhancements for the 5.8-Mrad ($T_2 = 60$ $\mu$s) and 24-Mrad ($T_2 = 35$ $\mu$s) samples were 5.0 and 3.4, respectively (Table 1), which indicates that the signal enhancement decreases as $T_2$ decreases.

### Time Dependence for Individual Spin Packets

To understand the source of the enhancements, the time dependence of the magnetization was calculated for individual spin packets. At low microwave power, the time dependence of the absorption component of the magnetization ($M_v$) is an FID-like signal. The signal starts at the time when the magnetic field modulation corresponds to the field position of the spin packet. The amplitude of the signal increases with $B_1$. At high $B_1$ an additional signal is observed that is very different from the low-power signals. Figure 2 shows the time dependence of $M_v$ calculated with $B_1 = 0.17$ G for spin packets with $T_1 = 200$ $\mu$s and $T_2 = 35$ $\mu$s, which corresponds to a saturation factor (Eq. [1]) $\sim 1 \times 10^{-5}$, and means that the normal in-phase signal would be severely saturated. The peak-to-peak modulation amplitude is 1 G, so the modulation field varies sinusoidally between +0.5 and −0.5 G. The calculations (Fig. 2) are shown for spin packets with differing offsets relative to the zero-point of the modulation field. For spin packets with $|\Delta B_0| < \sim 0.40$ G there is a weak oscillatory signal, similar to those observed at lower $B_1$. For example, for a spin packet with $\Delta B_0 = 0.2$ G an oscillation is initiated as the modulation field increases and passes through 0.2 G, which is superimposed on a second oscillation that is initiated as the modulation field decreases and again passes through 0.2 G (Fig. 2). For spin packets with $|\Delta B_0| > \sim 0.40$ G, an

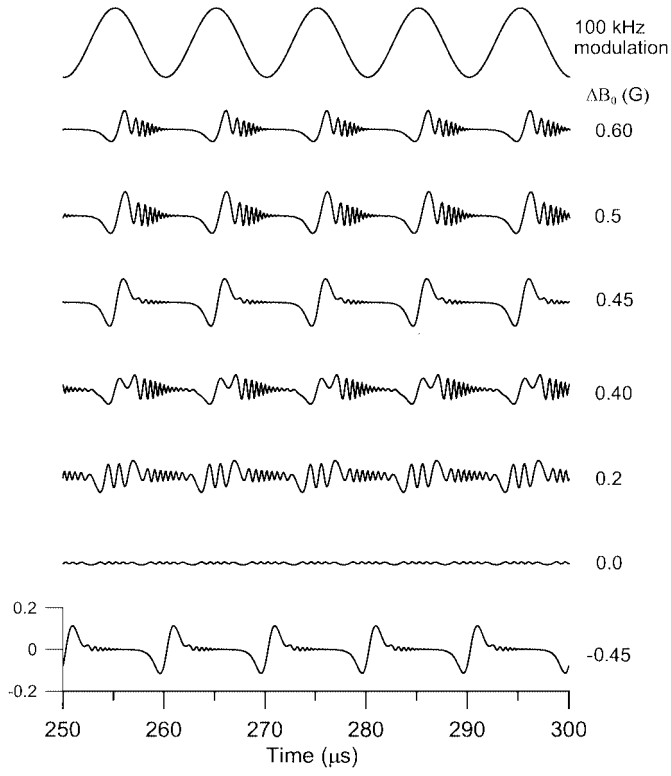


**FIG. 2.** Time evolution of $M_v$ for spin packets with different magnetic field offsets ($\Delta B_0$) from the zero-point of the modulation, calculated by numerically integrating the Bloch equations for 30 cycles with 1-G modulation amplitude at 100 kHz, $T_1 = 200$ $\mu$s, $T_2 = 35$ $\mu$s, and $B_1 = 0.17$ G. The segments shown are the final 5 cycles and reflect the steady state behavior. Each trace, except for the top trace that shows the time reference of the 100-kHz modulation, is plotted with the same $y$-axis scale. The scale, in arbitrary units, is shown for only one trace.

additional signal is observed at times that correspond to the extremes of the modulation cycle. For this large $B_1$ (0.17 G), the bandwidth is large enough to excite spins with $|\Delta B_0|$ substantially greater than 0.5 G (Fig. 2). Unlike the low-power signals, the position of the out-of-phase signal is independent of $|\Delta B_0|$; it occurs in the time interval where the magnitude of the modulation field is largest (Fig. 2). The signal shape is similar to a first derivative signal and is 90° out-of-phase with the magnetic field modulation. For $B_1 = 0.17$ G the maximum amplitude of the out-of-phase signal occurs for spin packets with $|\Delta B_0|$ between 0.45 and 0.5 G (Fig. 2). For spin packets with $|\Delta B_0|$ somewhat smaller than 0.45 G, the $B_1$ required to achieve the maximum out-of-phase signal is smaller than 0.17 G. These spin packets are impacted by the high $B_1$ and high modulation field for a longer total time so the $B_1$ required to have the same integrated effect on the spins is smaller than for spins with offsets closer to the extremes of the modulation.

Another perspective on the behavior of the spin system at high $B_1$ and large modulation field can be obtained by examining $M_z$. Figure 3 displays the time dependence of $M_z$ calculated for spin packets with the same $B_1$, relaxation times, and

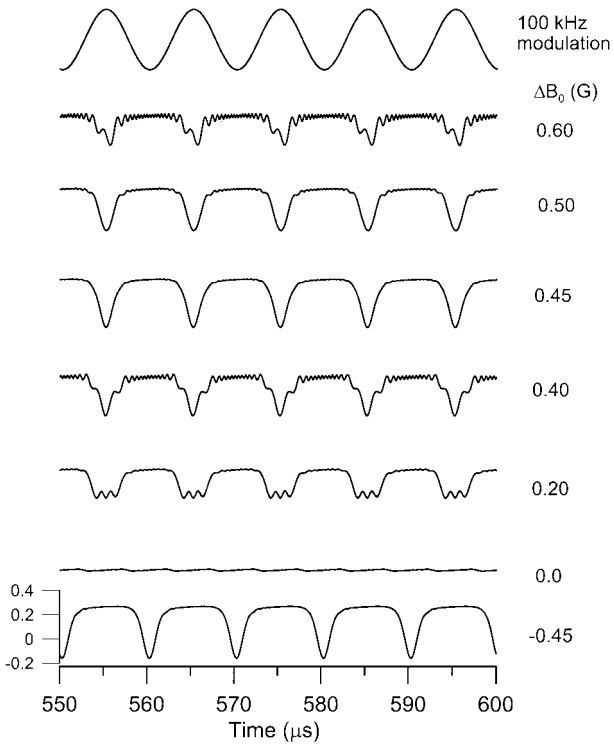


**FIG. 3.** Time evolution of $M_z$ for spin packets with different offsets ($\Delta B_0$) from the zero-point of the field modulation calculated by numerically integrating the Bloch equations. Parameters are the same as in Fig. 2. The segments shown are the final 5 cycles and reflect the steady state behavior. Each trace, except for the top trace that shows the time reference of the 100-kHz modulation, is plotted with the same $y$-axis scale. The scale, in arbitrary units, is shown for only one trace.

$|\Delta B_0|$ as in Fig. 2. Near the extremes of the modulation cycle $B_1$ dramatically tips the magnetization toward the $x$-$y$ plane. For the steady-state example shown in Fig. 3, $M_z$ for the spin packet with $\Delta B_0 = 0.45$ G decreases by about 20% at the extremes of the modulation cycle. For each value of $\Delta B_0$, the maximum effect of the modulation field on $M_z$ occurs at the same $B_1$ as the maximum effect on $M_v$. At constant $B_1$ the effect of the modulation field on $M_z$ depends on both $T_1$ and $T_2$. As $T_1$ increases, the spin packet becomes more saturated, and the fractional change in $M_z$ decreases. As $T_2$ increases, the amplitude of the magnetization vector increases because the spins do not dephase as much from one modulation cycle to the next.

## Waveforms Calculated as Sums of Spin Packet Contributions

The simulations for the individual spin packets show the conditions under which the out-of-phase signals are generated. However, to simulate the experimental waveforms the contributions from many spin packets must be summed. Individual spin packets are very narrow. For example, a spin packet with $T_2 = 30$ $\mu$s has a width at half height of 1.9 mG. Simulations were performed with 1000 to 3000 spin packets, including spin packets beyond the extremes of the modulation, which are within the bandwidth that is impacted by $B_1$. This bandwidth increases with increasing $B_1$. The number of spin packets included in the calculation was increased until the simulated waveform remained unchanged. The required number of spin packets increases as $T_2$ increases, because the linewidth of each packet decreases. The number of modulation cycles required for the waveform to come to a steady state also increases as $T_2$ increases. To reach a steady state required about 60 cycles for the sample with $T_2 = 35$ $\mu$s and 200 cycles for the sample with a $T_2 = 200$ $\mu$s. In addition, an exact field position for the calculation was important, especially in regions of the spectrum where the slope of the absorption spectrum changes rapidly. Less than a 0.1-G change in the magnetic field at which the calculation for position 1 (Fig. 1) was performed changed the simulated waveform dramatically.

Figure 4 shows the experimental and calculated waveforms as a function of $B_1$ at position 3 in the E′ spectrum (Fig. 1). Although the waveforms at high $B_1$ have much larger amplitude than at low $B_1$, the traces shown in Fig. 4 were scaled to the same amplitude to facilitate shape comparison. At each microwave power there is good agreement between the calculated and observed waveforms. At low $B_1$ the waveform has approximately the same shape as the modulation function, except that it is 180° out of phase. The change in phase occurs because the slope at this position in the spectrum is negative (Fig. 1). As $B_1$ is increased, the signal that approximates the shape of the modulation function increases and then decreases due to power saturation. In addition, as $B_1$ is increased, a signal with a derivative shape similar to that which was observed in the

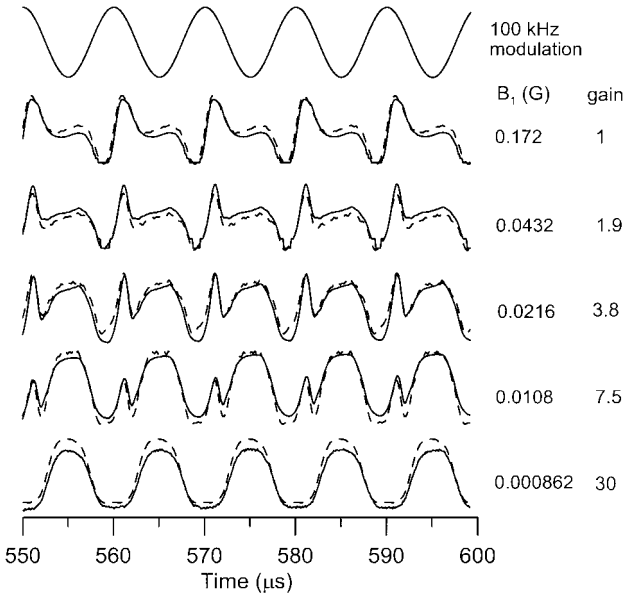


**FIG. 4.** Waveforms obtained with 1-G modulation amplitude and 100-kHz modulation frequency for the E′ signal in $SiO_2$ irradiated at 24.4 Mrad. Experimental waveforms (—) were obtained at position 3 (Fig. 1), which is where the first derivative is most strongly negative. Of the 60 modulation cycles that were calculated, the segments shown are the final 5 cycles, which reflects the steady state behavior. The amplitudes of the calculated waveforms (– – –) were scaled to match the experimental data. To facilitate comparisons the *y*-axis scales were adjusted to give the same signal amplitudes for all of the traces. The relative *y*-axis gains are shown beside each trace.

individual spin-packet calculations becomes increasingly dominant (Fig. 4).

The experimental and calculated waveforms were Fourier transformed to quantitate the amplitude of the signal at various harmonics of the modulation frequency and to analyze the phase of the components. Figure 5 shows the amplitude of the fundamental (100 kHz) components in the Fourier transformed experimental and calculated magnitude spectra at positions 1 and 3 (Fig. 1) in the spectrum of the 24.4-Mrad sample as a function of $B_1$. Since the amplitudes of the waveforms are in arbitrary units, the calculated data were scaled to match the experimental data at low $B_1$. The same scaling factor was used for the data at the two field positions. When the value of $T_2$ used to calculate the waveforms was set to the value obtained by the CPMG experiments, the shapes of the calculated waveforms were in good agreement with experiment. However, to match the experimentally observed intensities of the 100-kHz components as a function of $B_1$ it was necessary to adjust the value of $T_2$. As $B_1$ increased, the effective $T_2$ required to match the experimental signal intensity increased, and at high $B_1$ the effective $T_2$ was equal to $T_1$ (Fig. 5). When these adjustments were made, there was excellent agreement between calculated and observed signal intensity as a function of $B_1$ (Fig. 5). Similar agreement between calculated and experimental signal intensities was obtained for the 0.87- and 5.7-Mrad samples.

The relative amplitudes of the in-phase and out-of-phase components define the phase of the Fourier transformed signal. At low power the waveform is dominated by the in-phase contribution, but as $B_1$ is increased, the out-of-phase contribution becomes increasingly important. Thus the phase of the Fourier transformed signal varies from 0 to 90° as $B_1$ is increased (Fig. 6). There is good agreement between the phase of the signals for the calculated and observed waveforms as a function of $B_1$. However, at high $B_1$ if the spectrometer AFC is not exactly nulled, there can be mixing of absorption and dispersion contributions in the experimental data (*41*). Since the dispersion signal does not saturate as readily as the absorption, a dispersive component may contribute to greater discrepancy between calculated and experimental data at high $B_1$. The phase change as a function of $B_1$ is slightly different for the 3 samples (Fig. 6), but for $B_1 > \sim 0.2$ G the phase of the 100-kHz signal is 90° out-of-phase with the modulation.

At the magnetic field where the absorption is a maximum, the first derivative is zero (position 2 in Fig. 1). At this position the waveform has no fundamental component and only 2nd harmonic (or higher) components are observed, i.e., signals varying at 200 kHz (or higher). Figure 7 shows the magnitude of the experimental and simulated 2nd harmonic component of the waveform as a function of $B_1$ at position 2 (Fig. 1) in the

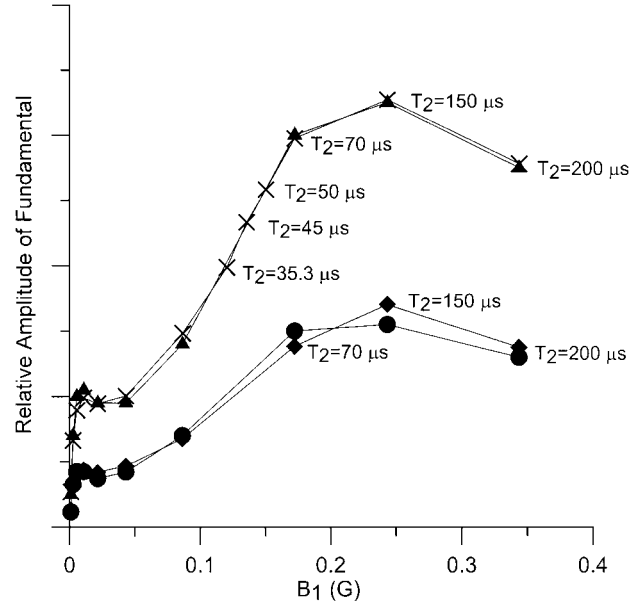


**FIG. 5.** Amplitude of the 100-kHz (fundamental) component in Fourier transforms of the waveforms for the E′ signal in the 24.4-Mrad sample: (●) experimental and (◆) calculated values at position 1; (▲) experimental and (**X**) calculated values at position 3 (Fig. 1). Ten cycles of experimental data were transformed. For the calculated waveforms the final 10 cycles out of 60 cycles calculated were transformed. The calculated values were scaled to match experiment at low $B_1$. For $B_1 > 0.12$ G, $T_2$ used in the simulation was adjusted to match the experimental intensity. The $T_2$ values that were used in the simulations for $B_1 > 0.12$ G are given adjacent to the corresponding data point. The lines connect the data points.

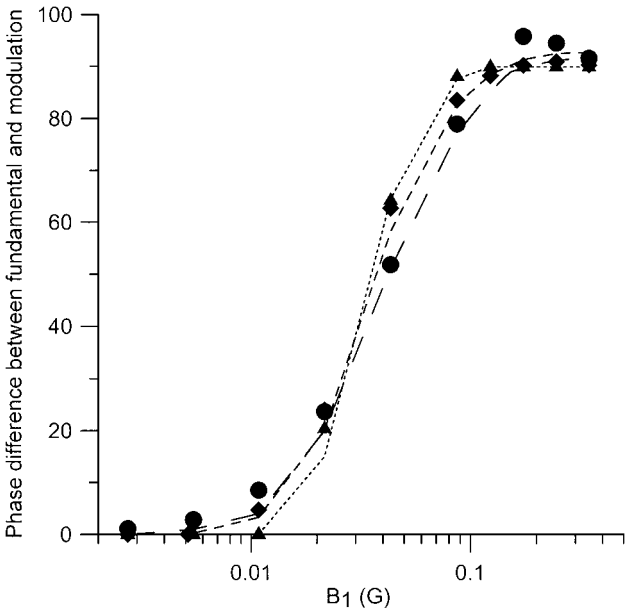


**FIG. 6.** Phase of the fundamental (100 kHz) component at position 3 in the spectrum (Fig. 1), in Fourier transforms of the waveforms obtained with 100-kHz modulation frequency and 1-G modulation amplitude: experimental (●) and calculated (—) for 24.4-Mrad sample; experimental (◆) and calculated (– – –) for 5.8-Mrad sample; experimental (▲) and calculated (· · ·) for 0.87-Mrad sample.

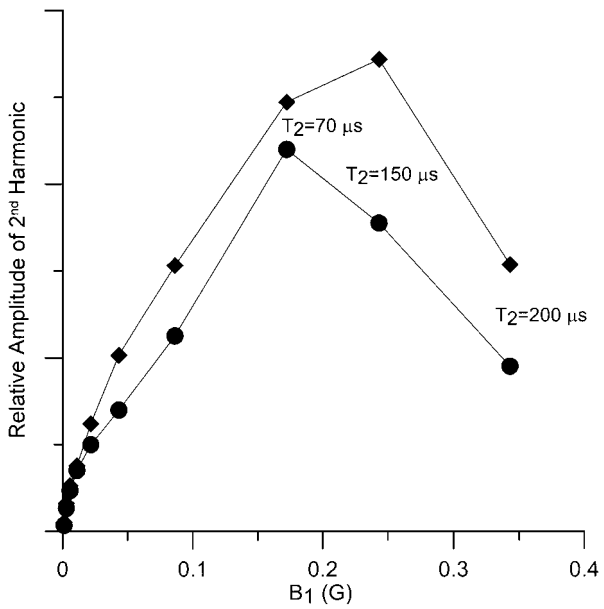


**FIG. 7.** Amplitude of the 2nd harmonic (200 kHz) component of the waveforms at position 2, as a function of $B_1$: experimental (●), calculated (◆). Ten cycles of experimental data were transformed. For the calculated waveforms the final 10 cycles out of 60 cycles calculated were transformed. The scaling factor that was determined in Fig. 5 to relate the calculated and experimental 90° out-of-phase signal intensities at 100 kHz also was used to scale the intensity of the 2nd harmonic (200 kHz) component in Fig. 7. For $B_1 > 0.12$ G, $T_2$ used in the simulation was adjusted to match the experimental intensity. The $T_2$ values that were used in the simulations are given adjacent to the corresponding data point. The lines connect the points.

spectrum of the 24-Mrad sample. The scaling factor that was determined in Fig. 5 to relate the calculated and experimental 90° out-of-phase signal intensities at 100 kHz also was used to scale the intensity of the 2nd harmonic (200 kHz) component in Fig. 7. The agreement between the amplitudes of the 2nd harmonic component in the calculated and experimental waveforms was not as good at high power as was observed for the fundamental component, but the overall trends in amplitude for the calculated and experimental values as a function of $B_1$ are similar.

The maximum amplitude of the 2nd harmonic component in Fig. 7 was obtained at about the same $B_1$ as the maximum amplitude of the fundamental components in Fig. 5. The sum of the fundamental components calculated at positions 1 and 3 in the spectrum (Fig. 1) would be approximately proportional to the peak-to-peak amplitude in a first-derivative CW spectrum. This sum is approximately equal to the 2nd harmonic signal at position 2, which predicts approximately equal signal intensities for the fundamental and 2nd harmonic signals.

## Impact of Modulation Frequency and Modulation Amplitude on Signal Enhancement

At a modulation amplitude of 1 G, the Fourier transforms of calculated and experimental waveforms as a function of $B_1$ for the 24-Mrad sample (Table 1) were compared at 25, 50, and 100 kHz. The $B_1$ required to achieve $T_2 = T_1$ increased linearly with modulation frequency because, as the modulation frequency is increased, the modulation field passes more rapidly over a spin packet. The maximum signal intensity (after optimizing $B_1$) increased with increasing modulation frequency. At 25 kHz the experiments no longer satisfy the condition that $T_1$ and $T_2$ be much longer than $1/\nu_m$. At low $B_1$ the signal amplitude increases with modulation amplitude up to about 1 G. Larger values of modulation amplitude do not increase signal amplitude because of the small spectral extent of the E′ signal (Fig. 1). At a modulation frequency of 100 kHz, Fourier transforms of calculated and experimental waveforms as a function of $B_1$ were compared for 0.25, 0.50, and 1.0 G modulation amplitudes. The $B_1$ required to achieve $T_2 = T_1$ increases linearly with modulation amplitude, because at the higher modulation amplitudes the modulation field (at constant modulation frequency) passes more rapidly over individual spin packets. After adjusting $B_1$ for maximum signal, signal amplitude increases with increasing modulation amplitude. Thus for the E′ center the maximum rapid-passage signal was observed with 1.0-G modulation at 100 kHz. Simulations suggest that signal intensity would increase at higher modulation frequencies. However, higher $B_1$ would be needed to achieve maximum signal at higher modulation frequencies. If source noise dominates at higher $B_1$ the increased signal may not result in increased signal-to-noise.

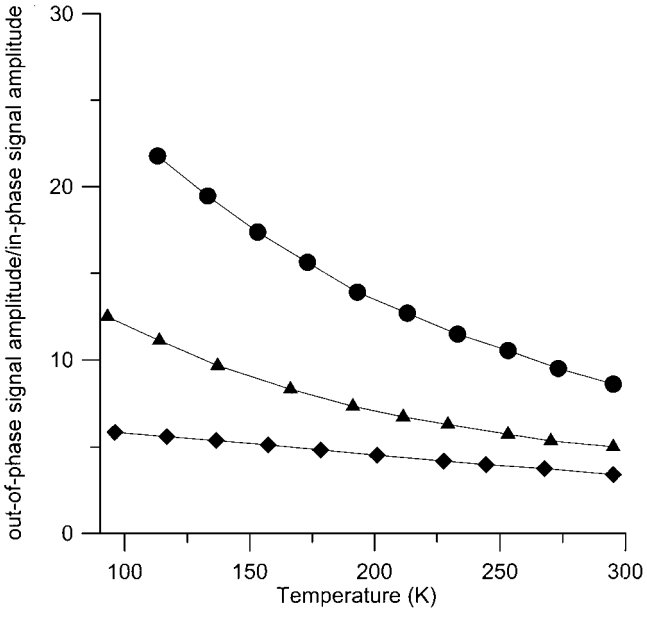


**FIG. 8.** Ratio of the maximum out-of-phase signal amplitude at each temperature to the maximum in-phase signal obtained at room temperature: 0.87 Mrad (●), 5.7 Mrad (▲), 24.4 Mrad (◆). $B_1$ was varied at each temperature to obtain the maximum signal. The largest in-phase signal was obtained at room temperature for all three samples. Data were obtained using 100-kHz modulation frequency and 1-G modulation amplitude.

## Low Temperature Studies

The out-of-phase E′ signals were examined as a function of temperature (Fig. 8). For these measurements the signal enhancement is defined as the ratio of the maximum out-of-phase signal that could be obtained by optimizing $B_1$ to the intensity of the maximum in-phase signal at room temperature. The room temperature signal was selected as the reference because the resulting value reflects the potential advantage in signal intensity that could be achieved by recording spectra at lower temperatures. $T_1$ for the E′ signal increased with decreasing temperature (*22*). For the samples studied here, about 25% larger $B_1$ was required to achieve the maximum out-of-phase signal at 100 K than at room temperature because of the increase in $T_1$. In addition, the increase in the relaxation times caused more signal saturation at high $B_1$, which reduced the signal enhancement. The signal enhancements at 100 K for all three samples were about twice as large as at room temperature (Fig. 8). Thus, the factor of three increase in signal enhancement calculated based on the change in the Boltzmann factor between 298 and 100 K is partially offset by increased saturation due to longer relaxation times and the larger $B_1$ required to obtain the maximum out-of-phase signals.

## Quantitation of Spin Concentration

As discussed in the Introduction, it is difficult to quantitate spin concentrations for the E′ centers based on the in-phase signal because it saturates so readily. If spectra are run under saturating conditions it is necessary to correct for the degree of saturation, which requires knowledge of $T_1$ and $T_2$ (Eq. [1]). The $T_1$ values for the E′ centers examined in this study showed little variation between samples, but $T_2$ varied substantially (Table 1). However, when the out-of-phase signals are recorded at high enough $B_1$ that $T_1 = T_2$, the saturation factor should be the same for all of the signals, and the observed signal amplitude is expected to be proportional to spin concentration. A plot of the peak-to-peak 90° out-of-phase signal amplitude/(gm sample) vs the spin concentration determined by ESE and low power CW spectra exhibits a linear correlation with a coefficient of determination, $R^2 = 0.9987$ (Fig. 9). Figure 9 includes data at room temperature for the three samples listed in Table 1 plus three other samples available in our laboratory. Out-of-phase signals for the six samples were recorded at room temperature with $B_1 = 0.33$ G (39 mW on the Varian E-9). This power was selected to achieve $T_1 = T_2$ for all of the samples, despite the fact that these conditions do not give the maximum out-of-phase signals for the samples with lower spin concentrations.

The out-of-phase signal enhancement for the E′ signal is greater at 77 K than at room temperature (Fig. 8), which suggests that the signal-to-noise might be better for quantitation at 77 K than at room temperature. For quantitation to be done without correcting individual integrals for power saturation requires operation under conditions where $T_1 = T_2$ and the assumption that $T_1$ is the same for all of the samples. For the samples with higher

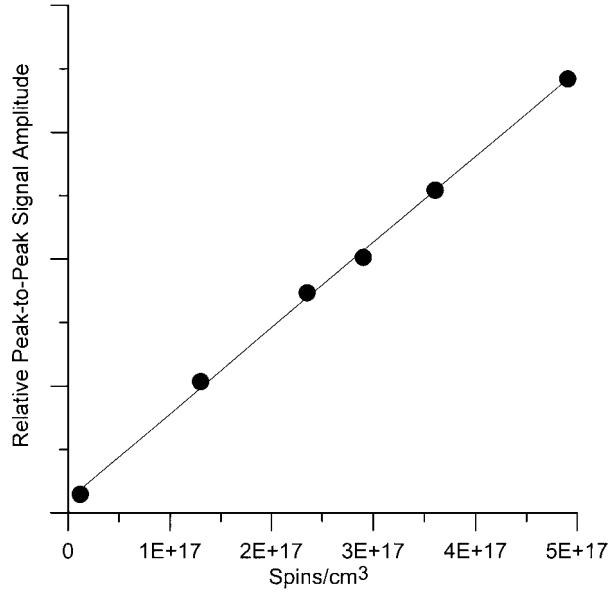


**FIG. 9.** Concentration dependence of the 90° out-of-phase signal for the E′ center. The spectra were obtained with 39-mW power ($B_1 = 0.33$ G), 1-G modulation amplitude, and 100-kHz modulation frequency. Coefficient of determination, $R^2 = 0.9987$. Spin concentrations were obtained by both instantaneous diffusion measurements and comparison of low power in-phase double-integrated CW signal intensity to that for a concentration standard.

spin concentration, the large increase in $T_1$ and small change in $T_2$ with decreasing temperature results in $T_2 \ll T_1$ at 77 K. As a result, the $B_1$ required to achieve $T_1 = T_2$ is significantly greater than the $B_1$ required to achieve maximum signal intensity for these samples. Up to this point we have assumed that the noise in a spectrum was unchanged as the signal was enhanced, which is true when the detector noise dominates and was the case for the room temperature measurements. However, the high values of $B_1$ required to achieve $T_1 = T_2$ for some of the samples at 77 K would require operation at powers greater than 45 mW, where source noise dominates on the Varian E9 and signal-to-noise is degraded. If however, quantitation were required only for samples at lower spin concentrations where $T_2$ is closer to $T_1$ at 77 K, the $B_1$ required to achieve $T_1 = T_2$ would not be so high and it could be advantageous to do the signal quantitation at 77 K rather than at room temperature. This would also be true on spectrometers with lower source noise.

## DISCUSSION

The spin-packet and waveform simulations showed that strong 90° out-of-phase signals are generated at high $B_1$ when $T_1$ and $T_2$ are longer than $1/\nu_m$(=10 $\mu$s at 100 kHz), but not when the relaxation times are much shorter than $1/\nu_m$. These are rapid-passage signals. These out-of-phase signals occur at the extremes of the modulation cycle, for spin packets with $|\Delta B_0|$ that is within about 0.2 G of the extremes of the modulation (Fig. 3). For these spin packets $B_1$ is of the order of the modulation field. To simulate the amplitude of the 100-kHz component of the experimental waveforms as a function of $B_1$, the effective value of $T_2$ was increased from the experimental (CPMG) value at low $B_1$ until it was equal to $T_1$ at high $B_1$ (Fig. 5). This increase in effective $T_2$ is consistent with Redfield's work on nuclear spin relaxation (*33*) and Hyde's analysis of CW saturation (*34*). The $B_1$ that was required to achieve $T_2 = T_1$ for these samples was about 0.3 G. The minimum $B_1$ that caused the effective $T_2$ to be larger than the experimental value increased as $T_2$ decreased (Fig. 5). Since higher spin concentrations result in shorter $T_2$, the same $B_1$ has a greater impact on effective $T_2$ at lower spin concentration.

In a normal unsaturated CW experiment the $B_1$ is so small that it causes minimal perturbation of the spin magnetization. However, in the high-power CW experiments ($B_1 > \sim 0.1$ G) the impact on the magnetization can be large and may be viewed analogous to a pulsed experiment. In a pulse experiment $B_1$ frequently is of the order of a Gauss. The spin packets for the E′ signal are very narrow (less than 2 mG). For small spin packet offsets, $\Delta B_0$, the modulation field is changing rapidly, so the residence time on a spin packet is small, and the magnetization is tipped by a relatively small amount. For larger spin packet offsets, for example, at $\Delta B_0 = 0.45$ G, the rate of change of the modulation field is slower so the residence time on a spin packet is greater. In addition, the magnitude of the modulation field at $\Delta B_0 = 0.45$ G is comparable to the $B_1$ values that were found to generate the large out-of-phase signals, which generates a "special case" for the magnetization (*33*). The magnetization is effectively "locked" in the rotating frame of the modulation field and the impact on the magnetization vector is large (Figs. 2 and 3).

### Signal Enhancement and Spin Concentration

Because higher $B_1$ is required to make $T_2 = T_1$ for samples with larger spin concentrations, the sample saturates more and the degree of enhancement is less for these samples than for samples with smaller spin concentrations. If the spin concentration is very high it takes a very high $B_1$ to make $T_2 = T_1$ and the saturation may outweigh the enhancement obtained by the increased $T_2$. In addition, phase noise from the source becomes a problem at high powers, which decreases signal-to-noise. For these reasons out-of-phase detection is most useful for samples with low spin concentrations.

### Comparison of Fundamental and 2nd Harmonic Detection

The 2nd harmonic detection of E′ signals at high $B_1$ has been used previously (*12, 13*) to improve signal-to-noise. The second harmonic signal is largest at the maximum in the absorption spectrum. Calculations show that for the E′ signal observed at 100 kHz with 1-G modulation amplitude, the second harmonic is maximized at about the same $B_1$ as is the fundamental signal detected 90° out-of-phase. In addition, the amplitudes of the fundamental and 2nd harmonic signals are about equal, which gives similar advantages in signal-to-noise. For 100-kHz modulation a potential disadvantage of the 2nd harmonic is that detection via a phase-sensitive detector would require a 200-kHz detector. The Bruker E-580 has the capability of 200-kHz detection for 2nd harmonic signals; however, Varian E-9 spectrometers only have the capability of 100-kHz detection for 2nd harmonic signals. Thus to use 2nd harmonic detection on the E-9 would permit a maximum modulation frequency of 50 kHz. Experimental and calculated data show that as the modulation frequency is decreased, the signal enhancement decreases.

### Determination of $B_1$

The calculated waveforms are strongly dependent on $B_1$ (Fig. 4). At high $B_1$ there are many harmonics in the experimental waveform so Fourier transforms of the waveforms are the most effective way to judge the agreement between simulation and experiment. In Fourier transforms of some of the simulated waveforms, the relative amplitudes of the fundamental through 7th harmonic were within 10% of values in the Fourier transforms of the experimental waveforms. For this reason, analysis of the waveforms for the E′ signal in irradiated $SiO_2$, combined with accurate measurements of the power incident on the resonator, could be a very accurate way to determine $B_1/\sqrt{W}$ for a resonator.

## CONCLUSION

Enhanced out-of-phase fundamental and second harmonic EPR signals were observed for the E′ center in irradiated $SiO_2$ at high $B_1$ using 100-kHz modulation and 1-G modulation amplitude. The signal enhancement was greatest for the samples with the lowest spin concentrations and was greater at 77 K than at room temperature. At high $B_1$ the intensity of the out-of-phase signal is proportional to spin concentration, which permits spin quantitation for the E′ centers. The quantitation of spin concentrations using out-of-phase detection at high power should be applicable to other systems with long $T_2$ relaxation times such as $P_b$ centers at $Si/SiO_2$ interfaces and defect centers in tooth dosimetry. In addition, simulating the waveforms for the E′ signal in irradiated $SiO_2$ can be an accurate way to measure $B_1/\sqrt{W}$ because the shape of the waveforms is very sensitive to $B_1$.

## ACKNOWLEDGMENTS

Financial support of this work by NIH Grant GM 21156 and NSF Grant 9986942 is gratefully acknowledged. Enhancing the signal-to-noise of EPR spectra for samples with long relaxation times, such as the defect centers generated by radiation, has been urged by many colleagues. We shared ideas with Ya. S. Lebedev (Moscow) regarding dosimetry measurements in 1995. Patrick Lenahan (Pennsylvania State University) encouraged our focus on signal-to-noise for irradiated $SiO_2$.

## REFERENCES

1. A. M. Portis, Rapid passage effects in electron spin resonance, *Phys. Rev.* **100,** 1219–1221 (1955).
2. J. S. Hyde, Magnetic resonance and rapid passage in irradiated LiF, *Phys. Rev.* **119,** 1483 (1960).
3. J. S. Hyde and L. R. Dalton, Very slowly tumbling spin labels: Adiabatic rapid passage, *Chem. Phys. Lett.* **16,** 568–572 (1972).
4. F. Bloch, Nuclear induction, *Phys. Rev.* **70,** 460 (1946).
5. M. Weger, Passage effects in paramagnetic resonance experiments, *Bell Syst. Tech. J.* **39,** 1013–1112 (1960).
6. C. Mailer and C. P. S. Taylor, Rapid adiabatic passage EPR of ferricytochrome c: Signal enhancement and determination of the spin-lattice relaxation time, *Biochim. Biophys. Acta* **232,** 195–203 (1973).
7. C. A. J. Ammerlaan and A. van der Wiel, The divacancy in silicon: Spin-lattice relaxation and passage effects in electron paramagnetic resonance, *J. Magn. Reson.* **21,** 387–396 (1976).
8. V. I. Gulin, S. A. Dikanov, Yu. D. Tsvetkov, R. G. Evelo, and A. J. Hoff, Very high frequency (135 GHz) EPR of the oxidized primary donor of the photosynthetic bacteria *Rb. sphaeroides* R-26 and *Rps. viridis* and of $YD^{\cdot}$ (signal II) of plant photosystem II, *Pure Appl. Chem.* **64,** 903–906 (1992).
9. S. Un, L.-C. Brunel, T. M. Brill, J.-L. Zimmermann, and A. W. Rutherford, Angular orientation of the stable tyrosyl radical within photosystem II by high-field 245-GHz electron paramagnetic resonance, *Proc. Natl. Acad. Sci. U.S.A.* **91,** 5262–5266 (1994).
10. B. J. Hales, A. E. True, and B. M. Hoffman, Detection of a new signal in the ESR spectrum of vanadium nitrogenase from Azotobacter vinelandii, *J. Amer. Chem. Soc.* **111,** 8519–8520 (1989).
11. W. J. Rink and Y. Shimoyama, Improved detection of EPR signals used in quartz dating, *Ancient TL* **9**(3), 33–36 (1991).
12. D. L. Griscom, Characterization of three E′-center variants in X- and γ-irradiated high purity $SiO_2$, *Nucl. Instrum. Methods Phys. Res. B* **1,** 481–488 (1984).
13. D. L. Griscom and M. Cook, $^{29}Si$ superhyperfine interactions of the E′ center: A potential probe of range-II order in silica glass, *J. Non-Cryst. Solids* **182,** 119–134 (1995).
14. V. E. Galtsev, O. Y. Grinberg, Y. S. Lebedev, and E. V. Galtseva, EPR dosimetry sensitivity enhancement by detection of rapid passage signal of the tooth enamel at low temperature, *Appl. Magn. Reson.* **4,** 331–333 (1993).
15. V. E. Galtsev, E. V. Galtseva, and Y. S. Lebedev, Optimal registration conditions for tooth EPR dosimetry at low accumulated dose, *Appl. Radiat. Isot.* **47,** 1311–1315 (1996).
16. V. E. Galtsev, E. V. Galtsev, O. Ya. Grinberg, and Ya. S. Lebedev, Human tooth dosimetry with enhanced sensitivity, *J. Radioanal. Nucl. Chem. Lett.* **186,** 35–45 (1994).
17. R. B. Clarkson and D. S. Leniart, Resolution of the proton hyperfine structure of di-*tert*-butyl nitroxide by 90° out-of-phase second harmonic detection, *Magn. Reson. Chem. Biol. Phys.* June (1979).
18. B. J. Gaffney and H. J. Silverstone, Simulation of the EMR spectra of high-spin iron in proteins, *Biol. Magn. Reson.* **13,** 1–55 (1993).
19. B. J. Gaffney, D. V. Mavrophilipos, and K. S. Doctor, Access of ligands to the ferric center in lipoxygenase-1, *Biophys. J.* **64,** 773–783 (1993).
20. J. A. Weil, A review of electron spin resonance spectroscopy and its application to the study of paramagnetic defects in crystalline quartz, *Phys. Chem. Minerals* **10,** 149–165 (1984).
21. R. H. Silsbee, Electron spin resonance (EPR) in neutron-irradiated quartz, *J. Appl. Phys.* **32**(8), 1459–1462 (1961).
22. J. G. Castle, Jr., D. W. Feldman, P. G. Klemens, and R. A. Weeks, Electron spin-lattice relaxation at defect sites; E′ centers in synthetic quartz at 3 kilo-oersteds, *Phys. Rev.* **130**(2), 577–588 (1963).
23. D. L. Griscom, E. J. Friebele, and G. H. Sigel, Jr., Observation and analysis of the primary $^{29}Si$ hyperfine structure of the E′ center in non-crystalline $SiO_2$, *Solid State Commun.* **15,** 479–483 (1974).
24. D. L. Griscom, E′ center in glassy $SiO_2$: Microwave saturation properties and confirmation of the primary $^{29}Si$ hyperfine structure, *Phys. Rev. B* **20**(5), 1823–1834 (1979).
25. M. G. Jani, R. B. Bossoli, and L. E. Halliburton, Further characterization of the $E_1'$ center in crystalline $SiO_2$, *Phys. Rev. B* **27**(4), 2285–2293 (1983).
26. B. T. Ghim, S. S. Eaton, G. R. Eaton, R. W. Quine, G. A. Rinard, and S. Pfenninger, Magnetic field and frequency dependence of electron spin relaxation times of the E′ center in irradiated vitreous silica, *J. Magn. Reson. A* **115,** 230–235 (1995).
27. P. M. Lenahan and J. F. Conley, Jr., What can electron paramagnetic resonance tell us about the $Si/SiO_2$ system? *J. Vac. Sci. Technol. B* **16**(4), 2134–2153 (1998).
28. P. M. Lenahan and J. F. Conley, Jr., A comprehensive physically based predictive model for radiation damage in MOS systems, *IEEE Trans. Nucl. Sci.* **45**(6), 2413–2423 (1998).
29. S. S. Eaton and G. R. Eaton, Irradiated fused quartz standard sample for time-domain EPR, *J. Magn. Reson. A* **102,** 354–356 (1993).
30. B. Bales and L. Kevan, Paramagnetic relaxation of silver species in γ-irradiated frozen aqueous species, *J. Chem. Phys.* **52**(9), 4644–4653 (1970).
31. D. P. Dalal, S. S. Eaton, and G. R. Eaton, The effects of lossy solvents on quantitative EPR studies, *J. Magn. Reson.* **44,** 415–428 (1981).
32. K. M. More, G. R. Eaton, and S. S. Eaton, Determination of $T_1$ and $T_2$ by simulation of EPR power saturation curves and saturated spectra: Application to spin-labeled iron porphyrins, *J. Magn. Reson.* **60,** 54–65 (1984).

*33.* A. G. Redfield, Nuclear magnetic resonance saturation and rotary saturation in solids, *Phys. Rev.* **98,** 1787–1809 (1955).

*34.* J. S. Hyde, Saturation of the magnetic resonance absorption in dilute inhomogeneously broadened systems, *Phys. Rev.* **119,** 1492–1495 (1960).

*35.* G. Feher, Electron spin resonance experiments on donors in silicon. I. Electronic structure of donors by the electron nuclear double resonance technique, *Phys. Rev.* **114,** 1219–1244 (1959).

*36.* R. W. Quine, G. R. Eaton, and S. S. Eaton, Pulsed EPR spectrometer, *Rev. Sci. Instrum.* **63,** 4251–4262 (1992).

*37.* G. A. Rinard, R. W. Quine, J. R. Harbridge, R. Song, G. R. Eaton, and S. S. Eaton, Frequency dependence of EPR signal-to-noise, *J. Magn. Reson.* **140,** 218–227 (1999).

*38.* S. Meiboom and D. Gill, Modified spin-echo method for measuring nuclear relaxation times, *Rev. Sci. Instrum.* **29,** 688–691 (1958).

*39.* W. H. Press, S. A. Teukolsky, W. T. Verrling, and B. P. Flannery, "Numerical Recipes in Fortran: The Art of Scientific Computing," 2nd ed., pp. 704–708, Cambridge Univ. Press, Cambridge, UK, 1992.

*40.* S. S. Eaton and G. R. Eaton, Relaxation times of organic radicals and transition metal ions, *in* "Biological Magnetic Resonance" (L. J. Berliner, S. S. Eaton, and G. R. Eaton, Eds.), Vol. 19, Chap. 2, Kluwer Academic/Plenum, New York (2000).

*41.* P. Ludowise, S. S. Eaton, and G. R. Eaton, A convenient monitor of EPR automatic frequency control (AFC) function, *J. Magn. Reson.* **93,** 410–412 (1991).